ENVIRONMENTAL RESEARCH
LETTERS

OPEN ACCESS

RECEIVED
20 January 2023

REVISED
19 May 2023

ACCEPTED FOR PUBLICATION
23 May 2023

PUBLISHED
19 June 2023

Original content from this work may be used under the terms of the Creative Commons Attribution 4.0 licence.

Any further distribution of this work must maintain attribution to the author(s) and the title of the work, journal citation and DOI.

LETTER

Radiation as the dominant cause of high-temperature extremes on the eastern Tibetan Plateau

Yinglin Tian[1], Sarosh Alam Ghausi[2], Yu Zhang[1], Mingxi Zhang[1], Di Xie[1], Yuan Cao[1], Yuantao Mei[1], Guangqian Wang[1], Deyu Zhong[1,*] and Axel Kleidon[2,*]

[1] State Key Laboratory of Hydroscience and Engineering, Key Laboratory of Hydrosphere Sciences of the Ministry of Water Resources, Department of Hydraulic Engineering, Tsinghua University, Beijing, 100084, People's Republic of China
[2] Biospheric Theory and Modelling, Max Planck Institute for Biogeochemistry, 07701 Jena, Germany
[*] Authors to whom any correspondence should be addressed.

E-mail: zhongdy@tsinghua.edu.cn and akleidon@bgc-jena.mpg.de

Keywords: temperature extremes, physical causality, surface energy balance, radiation, land–atmosphere interaction

Supplementary material for this article is available online

Abstract

Temperature extremes have been related to anomalies in large-scale circulation, but how these alter the surface energy balance is less clear. Here, we attributed high extremes in daytime and nighttime temperatures of the eastern Tibetan Plateau (ETP) to anomalies in the surface energy balance. We find that daytime high-temperature extremes are mainly caused by altered solar radiation, while nighttime ones are controlled by changes in downwelling longwave radiation. These radiation changes are largely controlled by cloud variations, which are further associated with certain large-scale circulations that modulate vertical air motion and horizontal cloud convergence. In addition, driven by a high-pressure system, strengthened downward solar radiation tends to decrease the snow albedo, which then plays an important role in reducing upward solar radiation, especially during winter and for compounding warm events. The results during winter and summer are generally similar but also present significant differences in terms of the contribution of variations in snow albedo, surface turbulent fluxes, and horizontal advection of cloud, which hence need further attention in simulating the high-temperature extreme events in the ETP. Our work indicates the importance to attribute different temperature extremes separately from the perspective of energy balance.

1. Introduction and hypotheses

In recent years, increasing trends have been observed in the frequency, intensity, duration, and spatial extent of warm extremes (Zhai and Pan 2003, Seneviratne *et al* 2014). These trends are projected to continue in the future (Sillmann *et al* 2013, Thiery *et al* 2021), with one of the most significant signals detected in the central and eastern Tibetan Plateau (ETP) (Yin *et al* 2019). Tibetan Plateau, regarded as the third pole on the Earth, can modulate the large-scale circulation features through thermal forcing and thereby affect the climate in and around it (Li *et al* 2018, Li *et al* 2020b). Since extreme events have profound influences on human life, economic cost, agriculture, ecosystems, and hydrology (Easterling *et al* 2000, UNDRR 2022), understanding the underlying mechanism is important to better forecast temperature extremes and reduce their detrimental impacts.

Previous studies have found that temperature extremes are frequently accompanied by distinct large-scale circulation patterns, such as cold spells or heatwaves in Europe and the North Atlantic Oscillation (NAO) (Scaife *et al* 2008, Guirguis *et al* 2011, Simmonds 2018, Li *et al* 2020a), warm Arctic and a pattern resembling the positive phase of NAO with a Ural blocking located at its eastern flank (Park *et al* 2015, Luo *et al* 2016, Park and Lee 2019, Tian *et al* 2022), and winter temperature extremes in China and the Arctic Oscillation (You *et al* 2013, Ding *et al* 2018). These linkages have previously been attributed to (1) the advection of warm air (Schumacher

© 2023 The Author(s). Published by IOP Publishing Ltd

et al 2019, Zhou and Yuan 2022) and the intrusion of moisture, which tend to enhance downward longwave radiation (Alekseev et al 2019); (2) the high-pressure system and thus clear-sky condition, which can amplify the downward solar radiation (Trigo et al 2004); (3) large-scale subsidence and adiabatic heating (Li et al 2021); and (4) local land–atmosphere interactions, especially through surface turbulent fluxes (Fischer et al 2007, Miralles et al 2014).

However, how the large-scale circulations are manifested in surface air temperature is still not clear in the Tibetan Plateau. The anomalously warm winter (2016/2017) is reported to be caused by both atmospheric dynamics (i.e. energy transport by convective and large-scale atmospheric motions) and regional heat budget (i.e. variations in albedo and surface turbulent heat fluxes) (Zhang et al 2022). Yet, the general quantitative attribution of sub-seasonal warm events is still inadequate. Therefore, our goal here is to better identify the main causes of the occurrence of intraseasonal extreme temperatures from the perspective of surface energy balance, which has been widely used in the study of land–surface interaction (e.g. Lu and Cai 2009, Lesins et al 2012, Gong et al 2017, Lee et al 2017, Zeppetello et al 2020, Sato and Simmonds 2021).

To do so, we first decompose the anomalies in the 2 m air temperature into the contribution of advective, diabatic, and adiabatic heating following the method of Röthlisberger and Papritz (2023). Considering that diabatic heating is the major cause of the extreme heat in the Tibetan Plateau (Röthlisberger and Papritz 2023), we further investigate positive temperature anomalies due to diabatic heating by looking at deviations in the climatological mean surface energy balance during the occurrence of high-temperature extremes, which are then linked to anomalies in atmospheric circulation. The surface energy perturbations relate to anomalies in net shortwave radiation (ΔR_s), downward longwave radiation (ΔR_{ld}), surface turbulent fluxes (ΔJ), and residuals (ΔQ, mostly due to changes in ground heat fluxes) (Lesins et al 2012, Lee et al 2017). While ΔR_s is generally related to variations in cloud cover and snow albedo, ΔR_{ld} is largely determined by cloud cover, atmospheric water vapor, and near-surface air temperature, as reflected in semi-empirical parameterizations (Brutsaert 1975, Crawford and Duchon 1999). As for the sensible and latent heat fluxes, their sum (ΔJ) tends to self-adapt as they are mostly constrained by the radiative forcing and thermodynamics (Kleidon et al 2014), while their partitioning is related to the soil moisture availability (Koster et al 2009). Compared with other terms, the magnitude of ΔQ is much less on the Tibetan Plateau (Su et al 2017). What this then means is that temperature anomalies are dominated by changes in radiation. Furthermore, daily maximum temperatures relate primarily to the magnitude of solar radiation, while daily minimum temperatures to longwave radiation (Zhao et al 2020). We can thus hypothesize that extremes in maximum temperature and minimum temperatures might be primarily related to changes in solar radiation and longwave radiation, respectively.

We test our hypothesis by evaluating high-temperature extremes of the ETP during the years from 1979 to 2018, using China meteorological station data combined with ERA-5 reanalysis data. Land–atmosphere interaction observations (Ma et al 2020) in conjunction with NASA CERES Syn1deg satellite dataset (CERES) are also adopted to cross-check the results. We first identify high-temperature extremes as those outside the 0%–95% range and calculate the anomalies in the surface energy balance during these periods. Then, the driver is further investigated by separating the effects on downward longwave radiation using a semi-empirical parameterization (Brutsaert 1975, Crawford and Duchon 1999) into contributions from atmospheric effective emissivity (controlled by cloud cover fraction and specific humidity) and air temperature (which is also taken as the atmospheric heat storage), which are derived with a more solid physical basis instead of purely empirical estimation. Since solar radiation has a strong diurnal variation and it also significantly influences the diurnal range of turbulent heat fluxes, the main causes for extremely warm days (WDs) and nights are likely to be different. We then relate these differences in radiation to the specific synoptic setting. Anticyclones are generally characterized by the absence of clouds, which favors the penetration of solar radiation during daytime and is likely to cause positive anomalies of maximum temperature, while cyclones are usually accompanied by more clouds and inhibit radiative cooling at night, thus possibly increasing the minimum temperature (Luo et al 2022). To relate the occurrence due to these synoptic conditions, we thus distinguish between three kinds of warm extremes: independent warm day (IWD) extremes, independent warm night (IWN) extremes, and compound warm (CW) extremes that show extremes for both maximum and minimum temperatures, similarly as defined in Chen and Zhai (2017) and Luo et al (2022).

This paper is organized as follows: section 2 describes how extremes in 2 m air temperature are identified and formulates our approach to estimating temperature deviations from anomalies in surface energy balance components. In the results section, we first present the decomposition of the anomalies in 2 m air temperature, with the contribution of diabatic heating further explained by variations in the surface energy balance, which are then related to the synoptic changes before and after the occurrence of the

extremes. After that, we discuss the potential limitations of our methodology, investigate the variations of the mechanisms of the heat extremes as heatwave evolves and among seasons, and finally describe some broader implications. We close with a brief summary and conclusions.

2. Data and methods

2.1. Study region and data

We focus our analysis on the ETP (ETP, 90°E–103E°, 27 N°–40 N°, as is indicated by the bold black rectangle in figure 3), which has a large number of weather stations (73 stations), while the western part (76°E–89 E°, 27 N°–40 N°), has only 13 stations.

To select the high-temperature extremes, the observed maximum and minimum 2 m air temperatures ($T_{\mathrm{Max,\,obs}}$ and $T_{\mathrm{Min,\,obs}}$) data from Dataset of Daily Climate Data from Chinese Surface Stations (V3.0) (National Meteorological Information Center 2019) during winter (DJF, December, January, and February) and summer (JJA, June, July, and August) spanning from 1979 to 2018 is used. For these station data, data quality control and homogeneity adjustment are performed using RclimDex (Zhang and Yang 2004) and RHtestsV3 software packages (Wang and Feng 2010), respectively.

To attribute the temperature anomalies, hourly data from ERA5 data (Hersbach *et al* 2018) are used, including 2 m temperature (T_a), skin temperature (T_s), surface downward solar radiation (R_{sd}), surface upward solar radiation (R_{su}), surface downward longwave radiation (R_{ld}), surface latent heat flux (LE), surface sensible heat flux (H), total cloud cover (f_c), surface water vapor pressure (e_a, which is calculated using dew point temperature), averaged soil moisture within 0–289 cm underground (SM), geopotential height on 500 hPa (Z500), vertical velocity on 500 hPa, surface 10 m U-wind speed (u_{10m}), surface 10 m V-wind speed (v_{10m}), surface pressure (p_s), total water vapor, snow albedo, and vertically integrated convergence of the fluxes of frozen cloud, liquid cloud, and moisture.

Before starting the analysis, we first compare the temperature anomalies from observation and ERA5 data during winter and summer (figures S1 and S2). Generally, good agreement can be observed between the two datasets ($\Delta T_{\mathrm{a,ERA5}}$ and $\Delta T_{\mathrm{a,obs}}$), especially in terms of maximum temperature anomalies ($R^2 \approx 0.9$), and the deviations are noted and analyzed in Text. S1.

Finally, to double-check the results, air temperature, radiation, and surface turbulent fluxes from land–atmosphere interaction observations (Y. *et al* 2020) and cloud cover from NASA CERES Syn1deg satellite dataset (CERES, Doelling *et al* 2013, 2016) are also adopted to repeat the analysis.

2.2. Identification of high-temperature extremes

High-temperature extremes are identified based on the following four steps using observed T_{Max} and T_{Min}, (i.e. $T_{\mathrm{Max,obs}}$ and $T_{\mathrm{Min,obs}}$):

(1) The seasonal cycle is removed by subtracting the multi-year average for every calendar day, and then the annual trend is removed by subtracting monthly-mean T_{Max} (also for T_{Min}) for each year from daily observations.
(2) High-temperature extremes for day and night are selected as those days at which regional-mean $T_{\mathrm{Max}} > T_{\mathrm{Max,\,95th}}$ for daytime extremes and $T_{\mathrm{Min}} > T_{\mathrm{Min,\,95th}}$ for nighttime extremes. The region-mean anomalies derived in this way are shown in figure S3.
(3) Consecutive extreme WDs or nights are merged to get the WD and warm night (WN) events while keeping at least three days separation between every two events. More than 95% of the high-temperature extreme events last no more than 3 d (tables S1 and S2).
(4) High-temperature extreme events are divided into three kinds: (1) IWD, when no WN event occurs within 24 h before or after a WD event, (2) IWN, when no WD event occurs within 24 h before or after a WN event, and (3) CW, when WN and WD events occur simultaneously in no more than 24 h apart from each other. The frequency and temperature evolution are shown in tables S1, S2, and figure S3. Since WDs precede WNs in more than 90% of the CW events, the other case in which compound events started with a WN are excluded from this work.

With the support of statistic investigation in figures S1 and S2, we then decompose the anomalies of air temperature and further analyze the related driver based on ERA5 data, using the dates at which the extremes occurred in the observed temperatures ($T_{\mathrm{max,obs}}$ and $T_{\mathrm{min,obs}}$).

2.3. Decomposition of changes in air temperature

According to Röthlisberger and Papritz (2023), temperature anomalies can be decomposed as,

$$\Delta T_a = \Delta T_{\mathrm{adiabatic}} + \Delta T_{\mathrm{advection}} + \Delta T_{\mathrm{diabatic}}, \quad (1)$$

where ΔT_a represents the anomaly of 2 m air temperature, the three terms on the right side of equation (1) are the contributions of adiabatic heating, heat advection, and diabatic heating, which can be further calculated as equations (2)–(4),

$$\Delta T_{\mathrm{adiabatic}} = \frac{\kappa T_a}{p_s}\omega, \quad (2)$$

$$\Delta T_{\mathrm{advection}} = \frac{\partial T_a}{\partial x}u_{10m} + \frac{\partial T_a}{\partial y}v_{10m} + \frac{\partial T_a}{\partial p}\omega, \quad (3)$$

$$\Delta T_{\text{diabatic}} = f\Delta T_s, \tag{4}$$

where $\kappa = 0.286$ is Poisson's constant, p_s is surface pressure, ω is the surface vertical velocity (which is calculated using pressure variation), u_{10m} and v_{10m} are surface 10 m wind velocity. Equation (4) is obtained with the hypothesis that the changes in air temperature due to diabatic heating can be calculated using skin temperature variation (ΔT_s), considering the consistency of variations in air and skin temperature (Lee *et al* 2017, Zeppetello *et al* 2020). f is the land–surface air temperature sensitivity coefficient to diabatic forcing, and we here assume $f = 1$ based on the work of Lee *et al* (2017) and Zeppetello *et al* (2020). With equation (4), we can further attribute $\Delta T_{\text{diabatic}}$ to anomalies in surface energy balance, which writes as,

$$(1-\alpha)R_{sd} + R_{ld} - R_{lu} - LE - H = Q, \tag{5}$$

where R_{sd} is the downward solar radiation, $\alpha = R_{su}/R_{sd}$ is the surface albedo (R_{su} is the upward solar radiation), R_{ld} is the downward flux of longwave radiation, R_{lu} is the emitted upward flux of longwave radiation, LE is surface latent heat flux, H is surface sensible heat flux, and Q the ground heat flux. Note that the radiation terms are downward positive and turbulent heat flux is upward positive. By using $R_{lu} = \sigma T_s^4$ for R_{lu} (with σ being the Stefan–Boltzmann constant) and differentiating equation (5), we can express ΔT_s as,

$$\Delta T_s = \frac{(1-\bar{\alpha})\Delta R_{sd} - \bar{R}_{sd}\Delta\alpha + \Delta R_{ld} - \Delta LE - \Delta H - \Delta Q}{4\sigma\overline{T_s}^3}. \tag{6}$$

In this way, changes in the skin temperature can be attributed to the six components represented by terms on the right-hand of equation (6).

Considering the significant role that R_{ld} plays in global warming, we further determine the driving factors of the anomaly in R_{ld} using the semi-empirical expression from Brutsaert (1975) and Crawford and Duchon (1999),

$$R_{ld} = \varepsilon_a \sigma T_a^4, \tag{7}$$

where ε_a is the effective atmospheric emissivity. By differentiating equation (7), we can then express an anomaly ΔR_{ld} as

$$\Delta R_{ld} = \sigma\overline{T_a}^4\Delta\varepsilon_a + 4\sigma\overline{\varepsilon_a}\overline{T_a}^3\Delta T_a, \tag{8}$$

and attribute these to either variations in atmospheric emissivity ($\Delta R_{ld,\varepsilon}$) or atmospheric heat storage ($\Delta R_{ld,T}$), which are the first and second term at the right hand of equation (8), respectively. The effective atmospheric emissivity is related to cloud fraction (f_c) and water vapor pressure (e_a) as in Brutsaert (1975) and Crawford and Duchon (1999),

$$\varepsilon_a = f_c + (1-f_c)\left(1.24\left(\frac{e_a}{T_a}\right)^{\frac{1}{7}}\right). \tag{9}$$

With equation (9), we can thus decompose changes in emissivity into contributions by cloud fraction ($\Delta\varepsilon_{f_c}$) or atmospheric humidity ($\Delta\varepsilon_{e_a}$) (corresponding to the first and second term at the right hand of equation (9), respectively; the term related to ΔT_a is relatively small in magnitude, thus is ignored here),

$$\Delta\varepsilon_a \approx \left(1 - \overline{1.24\left(\frac{e_a}{T_a}\right)^{\frac{1}{7}}}\right)\Delta f_c + \frac{1.24}{7}\frac{(1-\overline{f_c})}{(\overline{e_a})^{6/7}(\overline{T_a})^{1/7}}\Delta e_a. \tag{10}$$

3. Results

3.1. Decomposition of the air temperature

Considering that the increase in extreme heat events is stronger in winter than in summer over the ETP (Liu *et al* 2006), we here only present the results of winter in the main text, with the results of the summer season provided in Supplementary Information and analyzed in the Discussion section. Figure 1(a) shows the decomposition of the anomalies in air temperature during warm extreme events in winter, and the corresponding evolution is shown in figure S4. Generally, the extreme heat events in the winter ETP are controlled by diabatic heating, which increases the air temperature to around 2–4 K, with advection and diabatic heating contributing to less than 0.5 K. This is consistent with what Röthlisberger and Papritz (2023) has found in the ETP and can be explained by high altitude and thus stronger sensitivity of the radiation there.

Figure 1(b) attributed the diabatic heating term to variations in surface energy balance, and the changes in R_{ld} are further explained in figures 1(c) and (d) based on the semi-empirical equations. We find that independent extreme events during the day (IWD) are caused by increases in solar radiation, with the changes in albedo ($\Delta T_{-\alpha}$) and downward solar radiation (ΔT_{Rsd}) contributing around 40% and 60%, respectively. Although increases in air temperature can strengthen downward longwave radiation ($\Delta R_{ld,T}$), this positive anomaly is offset due to less atmospheric emissivity ($\Delta R_{ld,\varepsilon}$) during IWD. The nighttime extremes (IWN) are dominated by increases in downwelling longwave radiation (ΔT_{Rld}), which is mostly caused by enhanced emissivity ($\Delta R_{ld,\varepsilon}$) due to increased cloud cover ($\Delta\varepsilon_{f_c}$), while

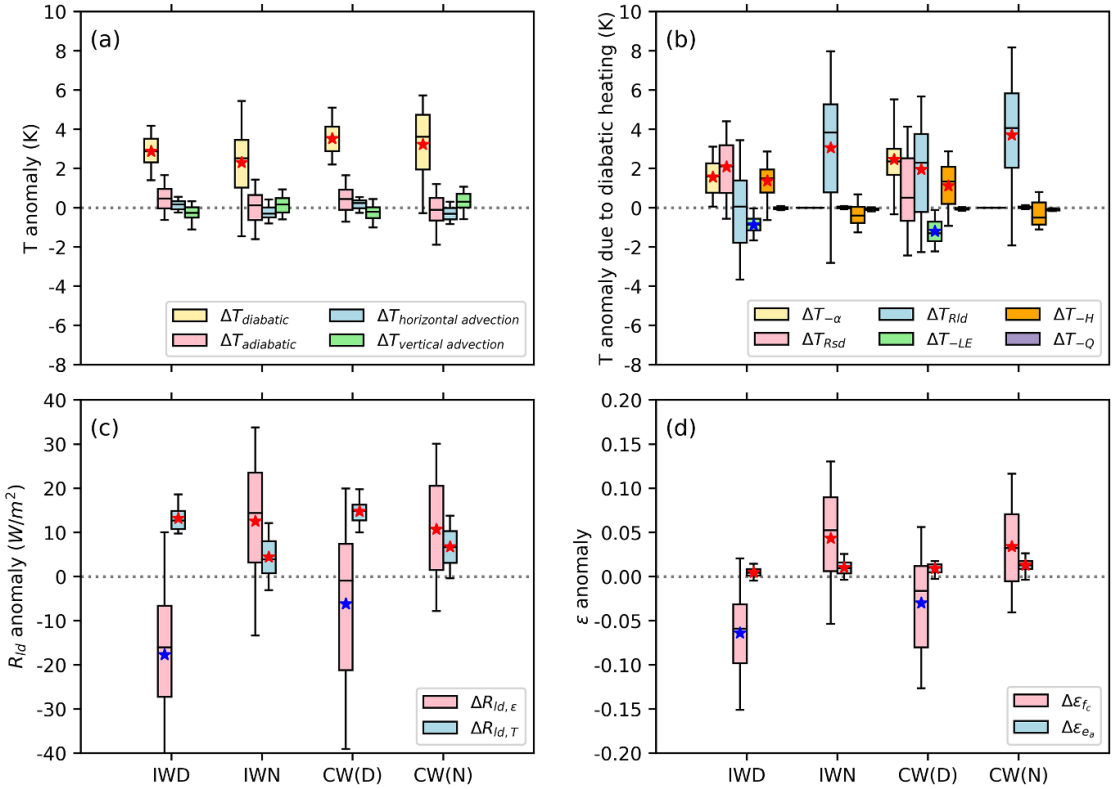

Figure 1. Decomposition of air temperature anomalies during high-temperature extreme events during winter (IWD = Independent Warm Days; IWN = Independent Warm Nights; CW: Compound events during (D) days and (N) nights). The average and spread among events of (a) regional-mean anomalies of air temperature due to diabatic heating ($\Delta T_{\text{diabatic}}$), adiabatic heating ($\Delta T_{\text{adiabatic}}$), horizontal heat advection ($\Delta T_{\text{horizontal advection}} = \frac{\partial T_a}{\partial x} u_{10m} + \frac{\partial T_a}{\partial y} v_{10m}$), and vertical heat advection ($\Delta T_{\text{vertical advection}} = \frac{\partial T_a}{\partial p}\,\omega$) (cf equations (1)–(4); (b) regional-mean anomalies of air temperature due to changes in the surface albedo ($\Delta T_{-\alpha}$), downward solar radiation (ΔT_{Rsd}), downward longwave radiation (ΔT_{Rld}), surface latent heat flux (ΔT_{-LE}), surface sensible heat flux (ΔT_{-H}), and ground heat flux (ΔT_{-Q}) (cf equation (6)); (c) regional-mean anomalies of R_{ld} due to changes in emissivity ($\Delta R_{\text{ld},\varepsilon}$) and near-surface air temperature ($\Delta R_{\text{ld},T}$) using Brutsaert's (1975) parameterization (cf equation (8)); (d) regional-mean anomalies of emissivity due to changes in cloud cover change ($\Delta \varepsilon_{f_c}$) and water vapor pressure ($\Delta \varepsilon_{e_a}$) using Crawford and Duchon's (1999) parameterization (cf equation (10)). Note that the vertical scale is different in the four panels. The box plot with stars has statistical significance at the 95% confidence level, with the significance test conducted following Lesk *et al* (2016). The stars indicate the event-mean value, with red and blue ones indicating heating and cooling effects, respectively. Boxplots show the range of all events present in table S1, no matter how many days the events last.

moisture anomalies ($\Delta \varepsilon_{e_a}$) add to changes in emissivity to a limited extent during IWN. As for the compound events (CW), its daytime witnesses both positive anomalies in shortwave and longwave radiation, with the former approximately twice as high as the latter and largely led by decreased surface albedo, while its nighttime condition resembles the setting during the independent WNs.

In comparison with radiation, a significantly positive change in turbulent heat fluxes ($\Delta T_{-LE} + \Delta T_{-H}$) does not appear to take place because the cooling and heating effect of ΔT_{-LE} and ΔT_{-H} generally compensate with each other, which hence plays no role in shaping the high-temperature extremes in the winter ETP.

3.2. Drivers of the anomalies in the surface energy balance

Considering the predominant role that anomalies in radiation play in shaping high-temperature extremes, the causes of radiation changes are further analyzed. To do so, we evaluate the time-mean value and evolution of the anomalies in related fields (figures 2 and S4), including components in surface energy balance, total cloud cover, total water vapor, snow albedo, snow moisture, vertical motion of air, and horizontal convergence of clouds and water vapor, which are then linked to anomalies in atmospheric circulation (figure 3). Figure 2 presents results related to events of one-day length because they account for most of the extreme events (tables S1 and S2), but longer events show similar patterns (figures S5–S8).

The IWD extreme events are accompanied by decreased snow albedo (figure 2(g)), which then increases the net solar radiation by around 8 W m^{-2} (figure 2(c)). In addition, IWD is preceded by a persistent anticyclone (figure 3), which favors large-scale subsidence (figure S4(e)) and suppresses the formation of clouds (figure 2(e)), thus increases the atmospheric transmittance and allows more solar radiation to penetrate (around 12 W m^{-2}) and heat the ground (figures 2(a) and (b)). It is notable that before

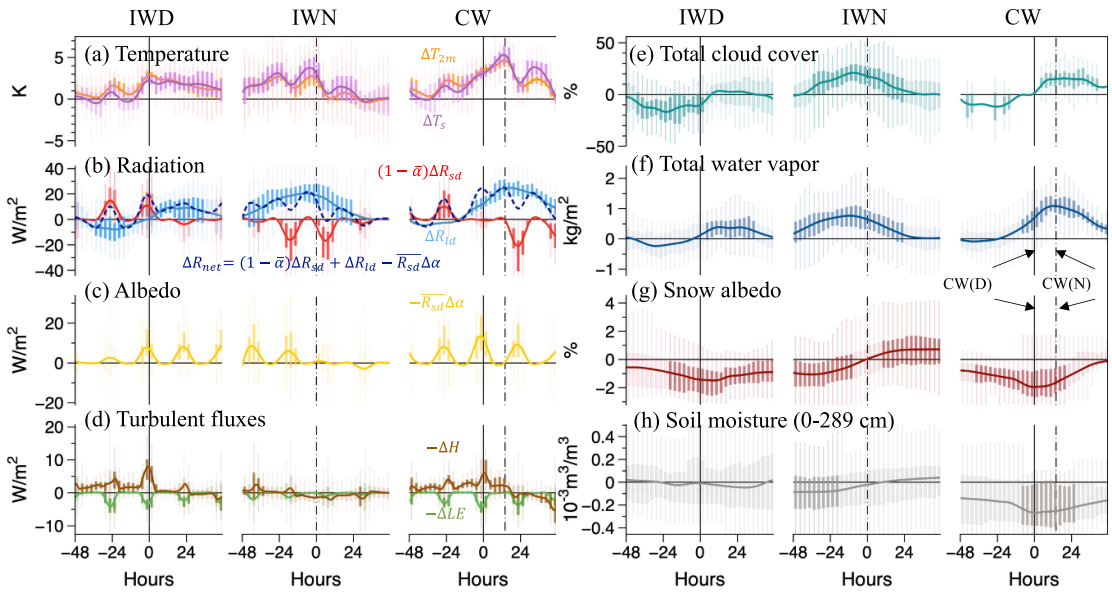

Figure 2. Temporal evolution of anomalies in (a) the skin and air temperature, (b) downward shortwave and longwave radiation, (c) solar radiation due to surface albedo changes, (d) surface latent and sensible heat fluxes, (e) cloud cover fraction, (f) total water vapor, (g) snow albedo, and (h) average soil moisture of 0–289 cm underground for one day-lasing independent warm day events (IWD), independent warm night events (IWN), and the compound warm events (CW) in winter. Results in figure (f) are vertically integrated values. Vertical solid and dashed-dotted lines mark the extremely warm day and night events, respectively. The box plot shows the mean value and ranges among events, with the upper and lower whistles presenting 95th and 5th, and the upper and lower edge of the box presenting 75th and 25th. Heavy lines are Loess fit lines. Heavy color boxes present the value with statistical significance at the 95% confidence level, with the significance test conducted following Lesk *et al* (2016). Note that the vertical scale and units are different in the different panels.

IWD, positive anomalies in the decreased cloud and increased downward solar radiation can already be observed, which contributes to melting the snow and reducing the surface albedo (figures 2(b) and (c)). Although the convergence of liquid and frozen clouds is also reduced during IWD (figures S4(f) and S4(g)), the anomalies are not significant, meaning that the subsidence of air is the dominant cause of cloud reduction. On the contrary, the IWN extreme events are controlled by a low-pressure system and upward motion, which favors the formation of cloud cover. Meanwhile, IWNs also experience a significantly strengthened convergence of cloud liquid or frozen water, which further adds to the total cloud cover. The increase in the cloud leads to an increase in downward longwave radiation by around 20 W m^{-2}. Different from independent warm extreme events, CW events witness an equatorward Rossby wave that originates from the Arctic and passes through the Eurasian continent. The propagation of this Rossby wave leads to a quick shift from high-pressure to a low-pressure system over the ETP, which not only favors large-scale subsidence and clear-sky conditions during daytime but also brings in more convergence of cloud-frozen water flux over the region in the following night, therefore strengthening the magnitude and extension of the warm extreme event. To be more specific, 24 h before the CW(D), enhanced downward solar radiation due to the overlying anti-cyclone leads to an increase in temperature and a decrease in snow albedo. After that, on the one hand, increased atmospheric heat storage adds to downward longwave radiation ($\Delta R_{\mathrm{ld},T}$, figure S4(d)), which prevents the surface to cool down; on the other, decreased snow albedo further enhances the absorption of solar radiation, which in return melts more snow cover. As a result, during CW(D), the positive anomalies in atmospheric storage and negative anomalies in the snow albedo contribute to the increase of surface radiation by around 5 W m^{-2} ($\Delta R_{\mathrm{ld},T}$) and 15 W m^{-2} ($-\bar{R}_{\mathrm{sd}}\Delta\alpha$), respectively. And then during CW(N), stronger atmospheric heat storage ($\Delta R_{\mathrm{ld},T}$) and emissivity ($\Delta R_{ld,\varepsilon}$) add to surface radiation by around 10 W m^{-2}, respectively.

To further ensure the robustness of our results, we repeat the analysis using the hourly data from the near-ground observation sites (Ma *et al* 2020, the site information is in table S3) in conjunction with CERES satellite data of cloud cover and radiation from 2005 to 2016 (Doelling *et al* 2013, 2016), and the results are shown in figure S9. Figure S9 generally verifies the robustness of the contribution of radiation to high-temperature extremes, but also stresses the necessity to use observation data for Tibetan Plateau analysis, especially in the western part with complex topography.

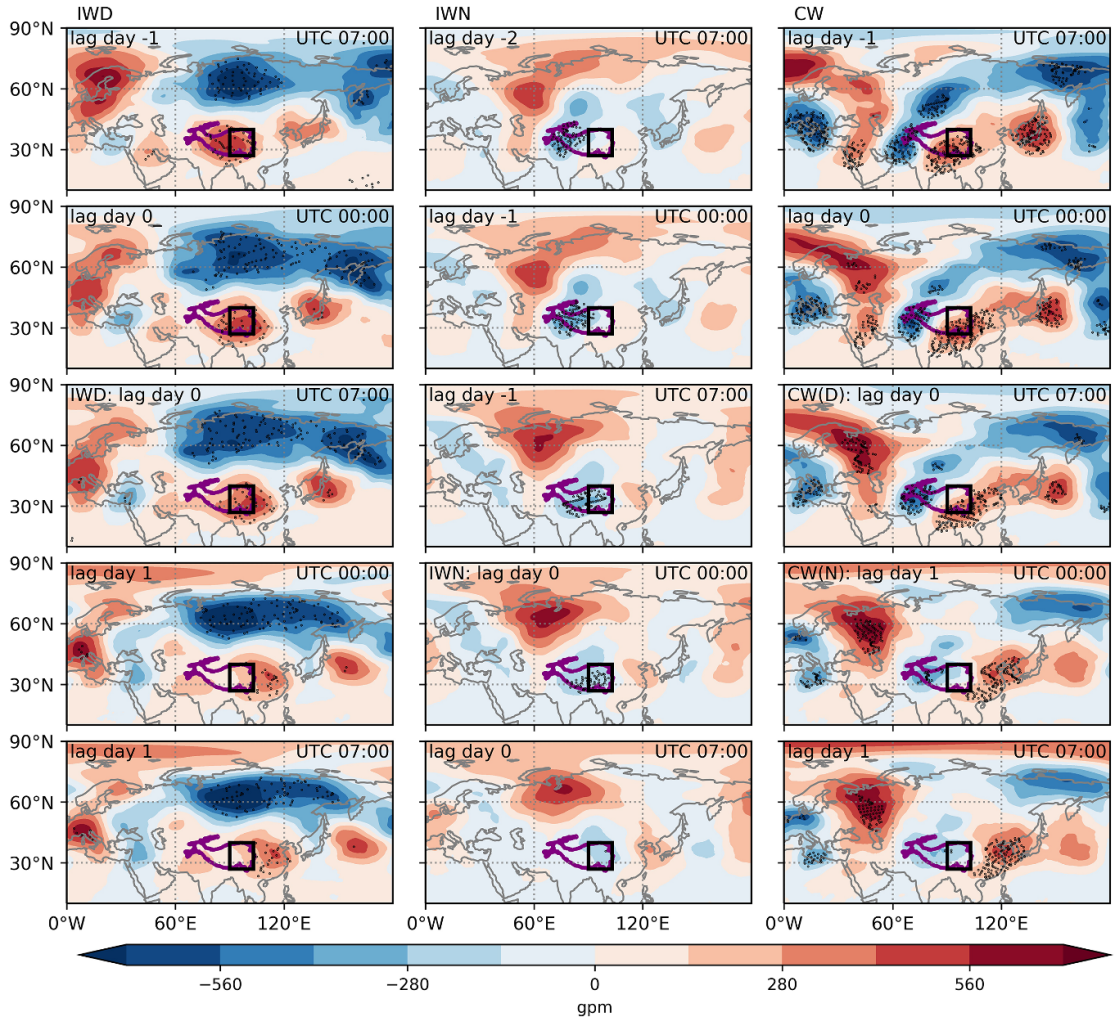

Figure 3. The evolution of geopotential height anomalies on 500 hPa before and after one day-lasting independent warm extreme events (IWD, the first column), independent warm night extremes (IWN, the second column), and compound events (CW, third column). Shading presents the anomalies of geopotential height, with the dots indicating values statistically significant at the 95% confidence level. The anomalies of geopotential height are plotted from 24 h before (the first row) to 24 h after (the last row) the IWD and CW events are triggered, while from 41 h before (the first row) to 7 h after (the last row) the IWN events. According to ERA5 hourly data, daily T_{max} and T_{min} over the winter Tibetan Plateau generally occur around UTC 07:00 and UTC 00:00, respectively. The solid purple polygon and black rectangle indicate the Tibetan Plateau and its eastern part.

4. Discussion

One of our most important assumptions is that the variation of the skin temperature can explain the diabatic contribution to changes in near-surface air temperature (i.e. $f = 1$, or $\Delta T_{\text{diabatic}} \approx \Delta T_s$). As shown in figure 1(a), most of the air temperature anomalies during extremes are explained by anomalies of the diabatic heating (i.e. $\Delta T_a \approx \Delta T_{\text{diabatic}}$). Furthermore, a great agreement can be observed in figures 2(a), S1 and S2 between ΔT_s and ΔT_a, with R^2 generally larger than 0.8 (i.e. $\Delta T_s \approx \Delta T_a$), which is also reported by Lee *et al* (2017), Zeppetello *et al* (2020). Hence, the dominance of diabatic heating in shaping high-temperature anomalies in the ETP and the consistency between variations in skin and air temperature together support our key hypothesis above. As a result, although the land–surface sensitivity ratio f is not exactly equal to 1, the bias does not seem to affect our interpretation. But more attention is in need for studies in other regions and time scales.

While we focus here on the role of anomalies in snow albedo and cloud cover and their effects on radiative fluxes, previous studies attributed extreme events to anomalies in heat advection, sensible heat flux, and adiabatic heating (Fischer *et al* 2007, Schumacher *et al* 2019, Li *et al* 2021). On the one hand, no significant positive changes in these three terms are found in figures 1(a) and (b), excluding these as the alternative direct driver of high-temperature extremes in winter ETP. On the other hand, by increasing air temperature (ΔT_a), these suggested alternatives could indirectly result in surface warming by enhancing the downwelling longwave radiation through $\Delta R_{ld,T}$, but not by $\Delta\varepsilon$, which results in the contribution $\Delta R_{ld,\varepsilon}$ (equation (8)).

However, our results show that $\Delta R_{\mathrm{ld},\varepsilon}$ generally contributes more than $\Delta R_{\mathrm{ld},T}$ (figure 1(c)). This implies that the warming at night over the ETP originates primarily due to a cloud cover change, and not due to the suggested alternatives. Therefore, our interpretation of the dominant effect of snow variation and cloud cover changes in shaping extreme temperatures of the ETP during winter appears to best explain our findings.

Here, we have only evaluated the triggering of extreme temperature events. This raises the question of how our findings relate to the mechanisms involved in developing heat waves. Previous studies have found that the mechanism for heat waves in Eastern Asia might vary with their life stages (Seo *et al* 2021). Hence, we present the analysis with a longer time window of events in figures S5–S8. We find that with the increasing life of the heat extreme events, the contribution of adiabatic heating will slightly increase, which might correspond to a more lasting downward motion. Moreover, with the heat extremes lasting longer, the contribution of heat storage to the downward longwave radiation ($\Delta R_{\mathrm{ld},T}$) is also larger, which prevents the temperature from cooling down after being heated during the daytime. And as the event develops, the sensible heat flux will gradually increase to add to the atmospheric heat storage, which is consistent with previous work (Miralles *et al* 2014, Schumacher *et al* 2019). What this shows is that while we evaluated the main drivers for extreme temperature events of the ETP, there may be other factors playing a role when it comes to heat waves, with the relative contributions changing as a heat wave develops.

The results above emphasize the importance of changes in cloud cover and snow albedo in winter warm extremes over the ETP and establish a mechanistic link to anomalies in the circulation, which also explains most parts of the warm events during summer. Besides, compared to the winter events, the summer cases have the following differences (figures S10–S16): first, the contribution of diabatic heating is more dominant, compared to advection and adiabatic heating; second, the anomalies of downward solar radiation (ΔR_{sd}) are relatively larger during extremely WDs, reaching as high as 70 W m^{-2}; third, under stronger radiative forcing, the surface turbulent heat fluxes have a cooling effect, with both latent and sensible heat flux significantly increased, which is not observed in winter due to lower magnitude of solar radiation and higher sensitivity of temperature to radiation forcing (larger $\frac{1}{4\sigma\overline{T_s}^3}$ in winter, seeing equation (6)) and thus lower Bowen ratio (Kleidon and Renner 2013); fourth, the effect of cloud increase on emitting more longwave radiation downward ($\Delta\varepsilon_{f_c}$) during WNs is weaker (which can be attributed to $(1-\overline{1.24(\frac{e_a}{T_a})^{\frac{1}{7}}})$ being less in the moister summer); and fifth, the anomalies in the horizontal convergence of cloud water have little significance during summer warm extreme events. These suggest that our interpretation may be specific to the region and seasons, with further effort in need of other temporal-spatial scales.

Our interpretation that anomalies in radiation are the main cause of high-temperature extremes has direct implications for expected trends with global warming. Observations show that nighttime temperatures respond more sensitively to an increase in the greenhouse effect than daytime temperatures, thereby reducing the diurnal temperature range (Easterling *et al* 1997, Kleidon and Renner 2017). This effect can be explained by the buffering effect of the convective boundary layer and the strong diurnal variation of turbulent fluxes on land (Kleidon and Renner 2017). Our results are consistent with these observations and interpretations. In the compound events, the radiative forcing is around 20 W m^{-2} during day and night (figure 2(b)), but the associated nighttime temperature anomaly is as high as 5 K while only 2.5 K during the daytime (figure 2(a)). This stronger temperature sensitivity at night can also be found during summer events. Since global warming is mostly associated with an increase in downward longwave radiation, we would expect that warm extremes at night become more frequent and intense than daytime extremes.

5. Summary and conclusions

We analyze high-temperature extreme events of the ETP and attributed these events to anomalies in the surface energy balance. We find that extremely WDs are caused by greater solar radiation warming because of less cloud cover and reduced snow albedo, which are associated with large-scale subsidence controlled by a persistent high-pressure system. Extremely WNs are mainly caused by increases in downward longwave radiation due to clouds related to the presence of a low-pressure system. Compound events are associated with an equatorward Rossby wave, which led to a change in the radiative conditions that favored both, extremely warm daytime and nighttime temperatures. Hence, in all cases, the direct cause for the extreme temperatures is radiation anomalies that are caused by changes in cloud cover and snow albedo associated with specific synoptic conditions. Nevertheless, it should also be noted that although the general mechanism of summer is consistent with winter, the contributions of snow albedo, surface turbulent fluxes, and cloud advection might vary with seasons. Therefore, the extent to which this interpretation holds more generally also in other time scales and regions would need to be explored in further research.

Data availability statement

All data that support the findings of this study are available from https://doi.org/10.17617/3.PLCJQE (Tian *et al* 2023).

Acknowledgments

This research was supported by the Second Tibetan Plateau Scientific Expedition and Research Program (Grant No. 2019QZKK0208) and the National Natural Science Foundation of China (52209026). This research resulted from a research stay of YLT in AK's research group. This stay was supported by China Scholarship Council as No. 202106210161.

We would like to thank Dr Yaoming Ma's lab from Institute of Tibetan Plateau Research Chinese Academy of Sciences for producing long-term land-surface observations on the Tibetan Plateau and making them openly accessible. And we also benefited a lot from the discussion with Dr Ma about the use of the observation data.

Open Research

Data presented in this manuscript are available through the National Tibetan Plateau Data Center (TPDC, 10.11888/Meteoro.tpdc.270910) of Tibetan Plateau observation data, the Copernicus Climate Change Service Climate Data Store (CDS, 10.24381/cds.adbb2d47 and 10.24381/cds.bd0915c6) for ERA5 reanalysis data, and the Clouds and the Earth's Radiant Energy System (NASA-CERES, https://ceres-tool.larc.nasa.gov/ord-tool/jsp/SYN1degEd41Selection.jsp) of SYN1deg satellite cloud data.

ORCID iDs

Yinglin Tian https://orcid.org/0000-0003-4134-1234
Sarosh Alam Ghausi https://orcid.org/0000-0003-2264-5486
Yu Zhang https://orcid.org/0000-0001-7317-3752
Mingxi Zhang https://orcid.org/0000-0003-2840-0885
Di Xie https://orcid.org/0009-0000-5359-5763
Yuan Cao https://orcid.org/0000-0002-4600-8943
Yuantao Mei https://orcid.org/0000-0002-9133-4000
Deyu Zhong https://orcid.org/0000-0003-4650-7221
Axel Kleidon https://orcid.org/0000-0002-3798-0730

References

Alekseev G, Kuzmina S, Bobylev L, Urazgildeeva A and Gnatiuk N 2019 Impact of atmospheric heat and moisture transport on the arctic warming *Int. J. Climatol.* **39** 3582–92

Brutsaert W 1975 On a derivable formula for long-wave radiation from clear skies *Water Resour. Res.* **11** 742–4

Chen Y and Zhai P 2017 Revisiting summertime hot extremes in China during 1961–2015: overlooked compound extremes and significant changes *Geophys. Res. Lett.* **44** 5096–103

Crawford T M and Duchon C E 1999 An improved parameterization for estimating effective atmospheric emissivity for use in calculating daytime downwelling longwave radiation *J. Appl. Meteorol.* **38** 474–80

Ding Z, Wang Y and Lu R 2018 An analysis of changes in temperature extremes in the three river headwaters region of the Tibetan Plateau during 1961–2016 *Atmos. Res.* **209** 103–14

Doelling D R, Sun M, Nguyen L T, Nordeen M L, Haney C O, Keyes D F and Mlynczak P E 2016 Advances in geostationary-derived longwave fluxes for the CERES synoptic (SYN1deg) product *J. Atmos. Ocean. Technol.* **33** 503–21

Doelling D R, Sun M, Nguyen L T, Nordeen M L, Morstad D, Nguyen C, Wielicki B A, Young D F and Sun M 2013 Geostationary enhanced temporal interpolation for CERES flux products *J. Atmos. Ocean. Technol.* **30** 1072–90

Easterling D R *et al* 1997 Maximum and minimum temperature trends for the globe *Science* **277** 364–7

Easterling D R, Evans J L, Groisman P Y, Karl T R, Kunkel K E and Ambenje P 2000 Observed variability and trends in extreme climate events: a brief review *Bull. Am. Meteorol. Soc.* **81** 417–26

Fischer E M, Seneviratne S I, Lüthi D and Schär C 2007 Contribution of land-atmosphere coupling to recent European summer heat waves *Geophys. Res. Lett.* **34** L06707

Gong T, Feldstein S and Lee S 2017 The role of downward infrared radiation in the recent Arctic winter warming trend *J. Clim.* **30** 4937–49

Guirguis K, Gershunov A, Schwartz R and Bennett S 2011 Recent warm and cold daily winter temperature extremes in the Northern Hemisphere *Geophys. Res. Lett.* **38** L17701

Hersbach H *et al* 2018 ERA5 hourly data on single levels from 1959 to present Copernicus Climate Change Service (C3S) Climate Data Store (CDS) (available at: https://cds.climate.copernicus.eu) (Accessed 3 June 2022)

Kleidon A and Renner M 2013 A simple explanation for the sensitivity of the hydrologic cycle to surface temperature and solar radiation and its implications for global climate change *Earth Syst. Dyn.* **4** 455–65

Kleidon A and Renner M 2017 An explanation for the different climate sensitivities of land and ocean surfaces based on the diurnal cycle *Earth Syst. Dyn.* **8** 849–64

Kleidon A, Renner M and Porada P 2014 Estimates of the climatological land surface energy and water balance derived from maximum convective power *Hydrol. Earth Syst. Sci.* **18** 2201–18

Koster R D, Schubert S D and Suarez M J 2009 Analyzing the concurrence of meteorological droughts and warm periods, with implications for the determination of evaporative regime *J. Clim.* **22** 3331–41

Lee S, Gong T, Feldstein S B, Screen J A and Simmonds I 2017 Revisiting the cause of the 1989–2009 arctic surface warming using the surface energy budget: downward infrared radiation dominates the surface fluxes *Geophys. Res. Lett.* **44** 10,654–61

Lesins G, Duck T J and Drummond J R 2012 Surface energy balance framework for Arctic amplification of climate change *J. Clim.* **25** 8277–88

Lesk C, Rowhani P and Ramankutty N 2016 Influence of extreme weather disasters on global crop production *Nature* **529** 84–87

Li M, Yao Y, Simmonds I, Luo D, Zhong L and Chen X 2020a Collaborative impact of the NAO and atmospheric blocking on European heatwaves, with a focus on the hot summer of 2018 *Environ. Res. Lett.* **15** 114003

Li W, Guo W, Qiu B, Xue Y, Hsu P-C and Wei J 2018 Influence of Tibetan Plateau snow cover on East Asian atmospheric circulation at medium-range time scales *Nat. Commun.* **9** 4243

Li X, Che T, Li X, Wang L, Duan A, Shangguan D, Pan X, Fang M and Bao Q 2020b CASEarth poles: big data for the three poles *Bull. Am. Meteorol. Soc.* **101** E1475–91

Li Y, Ding Y and Liu Y 2021 Mechanisms for regional compound hot extremes in the mid-lower reaches of the Yangtze River *Int. J. Climatol.* **41** 1292–304

Liu X, Yin Z, Shao X and Qin N 2006 Temporal trends and variability of daily maximum and minimum, extreme temperature events, and growing season length over the eastern and central Tibetan Plateau during 1961–2003 *J. Geophys. Res.* **111** D19109

Lu J and Cai M 2009 Seasonality of polar surface warming amplification in climate simulations *Geophys. Res. Lett.* **36** L16704

Luo D, Xiao Y, Yao Y, Dai A, Simmonds I and Franzke C L E 2016 Impact of Ural blocking on winter warm Arctic–cold Eurasian anomalies. Part I: blocking-induced amplification *J. Clim.* **29** 3925–47

Luo M, Lau N C and Liu Z 2022 Different mechanisms for daytime, nighttime, and compound heatwaves in southern China *Weather Clim. Extremes* **36** 100449

Ma Y *et al* 2020 A long-term (2005–2016) dataset of hourly integrated land–atmosphere interaction observations on the Tibetan Plateau *Earth Syst. Sci. Data* **12** 2937–57

Miralles D G, Teuling A J, van Heerwaarden C C and Vilà-guerau de Arellano J 2014 Mega-heatwave temperatures due to combined soil desiccation and atmospheric heat accumulation *Nat. Geosci.* **7** 345–9

National Meteorological Information Center 2019 Daily meteorological dataset of basic meteorological elements of china national surface weather station (V3.0) *National Tibetan Plateau Data Center* (available at: https://data.tpdc.ac.cn/en/data/52c77e9c-df4a-4e27-8e97-d363fdfce10a/) (Accessed 12 March 2020)

Park H-S, Lee S, Son S-W, Feldstein S B and Kosaka Y 2015 The impact of poleward moisture and sensible heat flux on arctic winter sea ice variability *J. Clim.* **28** 5030–40

Park M and Lee S 2019 Relationship between tropical and extratropical diabatic heating and their impact on stationary-transient wave interference *J. Atmos. Sci.* **76** 2617–33

Röthlisberger M and Papritz L 2023 Quantifying the physical processes leading to atmospheric hot extremes at a global scale *Nat. Geosci.* **16** 210–6

Sato K and Simmonds I 2021 Antarctic skin temperature warming related to enhanced downward longwave radiation associated with increased atmospheric advection of moisture and temperature *Environ. Res. Lett.* **16** 064059

Scaife A A, Folland C K, Alexander L V, Moberg A and Knight J R 2008 European climate extremes and the North Atlantic Oscillation *J. Clim.* **21** 72–83

Schumacher D L, Keune J, van Heerwaarden C C, Vilà-guerau de Arellano J, Teuling A J and Miralles D G 2019 Amplification of mega-heatwaves through heat torrents fuelled by upwind drought *Nat. Geosci.* **12** 712–7

Seneviratne S I, Donat M G, Mueller B and Alexander L V 2014 No pause in the increase of hot temperature extremes *Nat. Clim. Change* **4** 161–3

Seo Y-W, Ha K-J and Park T-W 2021 Feedback attribution to dry heatwaves over East Asia *Environ. Res. Lett.* **16** 064003

Sillmann J, Kharin V V, Zwiers F W, Zhang X and Bronaugh D 2013 Climate extremes indices in the CMIP5 multimodel ensemble: part 2. future climate projections *J. Geophys. Res.* **118** 2473–93

Simmonds I 2018 What causes extreme hot days in Europe? *Environ. Res. Lett.* **13** 071001

Su J, Duan A and Xu H 2017 Quantitative analysis of surface warming amplification over the Tibetan Plateau after the late 1990s using surface energy balance equation *Atmos. Sci. Lett.* **18** 112–7

Thiery W *et al* 2021 Intergenerational inequities in exposure to climate extremes *Science* **374** 158–60

Tian Y, Zhang Y, Zhong D, Zhang M, Li T, Xie D and Wang G 2022 Atmospheric energy sources for winter sea ice variability over the North Barents–Kara Seas *J. Clim.* **35** 5379–98

Tian Y, Zhong D, Wang G and Kleidon A 2023 Radiation as the dominant cause of high-temperature extremes on the Eastern Tibetan Plateau *Datasets and Figures* Version V1 (Edmond) (https://doi.org/10.17617/3.PLCJQE)

Trigo R M, Trigo I F, DaCamara C C and Osborn T J 2004 Climate impact of the European winter blocking episodes from the ncep/ncar reanalyses *Clim. Dyn.* **23** 17–28

UNDRR, U. N. O. f. D. R. R. 2022 Heatwaves: addressing a sweltering risk in Asia-Pacific vol 37 (available at: www.undrr.org/publication/heatwaves-addressing-sweltering-risk-asia-pacific)

Wang X L and Feng Y 2010 RHtestsV3 User Manual, UserManual.doc *Climate Research Division, Science and Technology Branch* (Toronto, ON: Environment Canada) pp 26 (available at: http://cccma.seos.uvic.ca/ETCCDMI/RHtest/RHtestsV3)

Yin H, Sun Y and Donat M G 2019 Changes in temperature extremes on the Tibetan Plateau and their attribution *Environ. Res. Lett.* **14** 124015

You Q, Ren G, Fraedrich K, Kang S, Ren Y and Wang P 2013 Winter temperature extremes in China and their possible causes *Int. J. Climatol.* **33** 1444–55

Zeppetello L R V, Tétreault-Pinard É, Battisti D S and Baker M B 2020 Identifying the sources of continental summertime temperature variance using a diagnostic model of land–atmosphere interactions *J. Clim.* **33** 3547–64

Zhai P and Pan X 2003 Trends in temperature extremes during 1951–1999 in China *Geophys. Res. Lett.* **30** 1913

Zhang T, Deng Y, Chen J, Yang S, Gao P and Zhang H 2022 Disentangling physical and dynamical drivers of the 2016/17 record-breaking warm winter in China *Environ. Res. Lett.* **17** 074024

Zhang X and Yang F 2004 RClimDex (1.0) user manual *Clim. Res. Branch Environ. Can.* **22** 13–14 (available at: http://etccdi.pacificclimate.org/software.shtml)

Zhao X, Liu C and Yang N 2020 Diurnal and seasonal variations of surface energy and CO2 fluxes over a site in western Tibetan Plateau *Atmosphere* **11** 260

Zhou S and Yuan X 2022 Upwind droughts enhance half of the heatwaves over North China *Geophys. Res. Lett.* **49** e2021GL096639